

Geophysical Research Letters®



RESEARCH LETTER

10.1029/2024GL108512

Key Points:

- Coupled model intercomparison project (CMIP6) models underestimate midlatitude ocean surface wind speed compared to spaceborne microwave radiometers
- Simulated ocean surface wind speed bias scales with model resolution at a magnitude strongly influenced by meteorology
- Ocean surface wind speed bias is most correlated with resolution in western boundary currents

Supporting Information:

Supporting Information may be found in the online version of this article.

Correspondence to:

G. Werapitiya,
wgeethma@uwyo.edu

Citation:






Werapitiya, G., McCoy, D., Elsaesser, G., Field, P., & Rahimi, S. (2024). Meteorology modulates the impact of GCM horizontal resolution on underestimation of midlatitude ocean wind speeds. *Geophysical Research Letters*, 51, e2024GL108512. <https://doi.org/10.1029/2024GL108512>

Received 26 JAN 2024

Accepted 19 JUN 2024

© 2024 Crown copyright and The Author(s). This article is published with the permission of the Controller of HMSO and the King's Printer for Scotland. This is an open access article under the terms of the [Creative Commons Attribution-NonCommercial-NoDerivs License](#), which permits use and distribution in any medium, provided the original work is properly cited, the use is non-commercial and no modifications or adaptations are made.

Meteorology Modulates the Impact of GCM Horizontal Resolution on Underestimation of Midlatitude Ocean Wind Speeds

Geethma Werapitiya¹ , Daniel McCoy¹ , Gregory Elsaesser² , Paul Field³ , and Stefan Rahimi¹ 

¹University of Wyoming, Laramie, WY, USA, ²Goddard Institute for Space Studies, Columbia University/NASA, New York, NY, USA, ³Met Office, Exeter, UK

Abstract We utilize ocean 10-m wind speed (U_{10m}) from the microwave Multi-sensor Advanced Climatology data set to examine the coupling between convective cloud and precipitation processes, synoptic state, and U_{10m} and to evaluate the representation of U_{10m} in global climate models (GCMs). We find that midlatitude U_{10m} is underestimated by GCMs relative to observations. We examine two potential mechanisms to explain this model behavior: cold pool formation in cold air outbreaks (CAOs) associated with downdrafts that enhance U_{10m} and sea surface temperature (SST) gradients affecting U_{10m} through thermally forced surface winds at regional scales. When the effects of the CAO index (M) and SST gradients on U_{10m} are accounted for, a relationship between GCM horizontal resolution and U_{10m} appears. The strongest correlation between resolution and U_{10m} is over the western boundary currents characterized by frequent CAOs atop strong SST gradients which drives the strongest surface fluxes on Earth.

Plain Language Summary Surface wind drives the exchange of momentum and energy between the atmosphere and ocean, forcing movement of ocean surface water that impacts the circulation responsible for transporting heat and carbon. It is thus important to study how well global climate models (GCMs) simulate near surface winds. Here, we show an underestimation of ocean surface wind in the latest-generation of GCMs and examine how an underestimation of ocean surface winds covaries with biases in surface temperature and fine-scale precipitation-driven circulations. We show the effect of model horizontal grid resolution on the wind speed bias and analyze surface wind speed bias occurrence in western boundary currents.

1. Introduction

Near surface wind speed is key to our understanding of the atmospheric state. It is critical to topics ranging from the availability of wind energy over the oceans (Possner & Caldeira, 2017), to how climate is affected through air sea exchanges of heat and gas (Fu et al., 2019), and the transition from shallow to deep convection (Elsaesser & Kummerow, 2013). Surface wind speed also affects dust emissions (Evan, 2018) and is important for setting the cloud feedback (Bodas-Salcedo et al., 2019). Surface winds play an integral role in the Earth's energy and hydrological cycles by setting the atmospheric and oceanic circulation (Alexander & Scott, 1997; Hartmann, 2016). Wind speed magnitude and direction impacts the wind stress that serves as a dominant energy source for the kinetic energy driving the ocean circulation (Ferrari & Wunsch, 2009). The drivers of variability in surface wind speed are complex and include both large scale variability in the atmosphere and processes that are internal to the boundary layer.

The most direct way that surface wind affects the climate system is by setting the flux of energy and momentum between the surface and the atmosphere. This flux can be approximated using the bulk formulas for sensible heat (SH), latent heat (LH) fluxes and momentum fluxes (M):

$$SH = C_p \rho C_{DH} U_r (T_s - T_a)$$

$$LH = L \rho C_{DE} U_r (q_s - q_a)$$

$$M = \rho C_{DM} U_r^2$$

where C_p and ρ are the specific heat at constant pressure and density of air; L is the LH of vaporization; C_{DH} and C_{DE} are the heat and moisture flux coefficients, C_{DM} is the momentum exchange coefficient; U_r is the mean wind speed at the standard height; and T and q are the air temperature and specific humidity. Subscripts s and a indicate values for the surface and the air at the reference level respectively. These formulas are used in global climate models (GCMs) to compute heat and momentum fluxes. The accurate representation of surface wind speed is critical to coupling between the atmosphere, ocean, and land surface in GCMs.

Ocean surface winds have an extensive observational record because of their importance to weather, energy, and global climate. Buoys provide an in-situ network of observations of ocean surface wind speed. Remote sensing of surface winds via satellites using passive and active instruments has been carried out for decades across global oceans (F. J. Wentz et al., 2017), expanding observational coverage beyond buoy-based point measurements. Satellite observations of ocean surface winds can be made using microwave radiometers and scatterometers (Fu et al., 2019; F. J. Wentz et al., 2017) as well as microwave altimeters (F. J. Wentz & Ricciardulli, 2011; Young, Zieger, & Babanin, 2011; Young, Babanin, & Zieger, 2011) and synthetic aperture radar (SAR) (Sikora et al., 2006).

Because ocean surface wind speed is crucial to our understanding of climate, realistic prediction of ocean surface wind speed by GCMs is essential to offering accurate predictions of future climate (McMonigal et al., 2023). Krishnan and Bhaskaran (2020) compared surface wind speed in Coupled Model Intercomparison Project Phase 5 (CMIP5) GCMs in the Bay of Bengal region with buoy observations for moderate winds yielding a correlation of 0.65 and maximum underestimation and overestimation of 2.5 m/s and 1.5 m/s, respectively. Shen et al. (2022) evaluated the global terrestrial near surface windspeed in 22 CMIP6 models relative to the US Air Force Global Surface Summary of the Day database and found biases ranging from -1 m/s to 1 m/s. Morim et al. (2020) found biases in CMIP5 multi-model ensemble mean wind speed relative to ERA-interim reanalysis data ranging from -2 m/s to 1.5 m/s. Clearly, there is substantial regional and global variation in simulated wind speed, and it is necessary to continue to evaluate the ocean surface wind speed discrepancies between GCMs and observations.

The ability of a given GCM to resolve features impacts the simulated surface wind speed across scales from global features (Chelton et al., 2004), to regional features (Chu, 1989; Small et al., 2008). At the regional scale, surface wind speed is affected by features such as ocean fronts and eddies (Small et al., 2008). The sea surface temperature (SST) gradient can affect the thermal forcing at the surface (Chu, 1989). Mesoscale SST features and SST fronts have a significant effect on wind speed and direction, particularly in western boundary currents (O'Neill et al., 2010; Seo et al., 2023). Poorly-resolved surface gradients can affect the representation of surface wind in GCMs through this process (Maloney & Chelton, 2006). Surface wind anomalies driven by strong SST gradients can lead to Ekman heat transport anomalies that ultimately affect the heat content variability in the upper ocean (Bellucci et al., 2021). Hence, evaluating the SST gradients' impact on surface wind is relevant to both meteorological and climate research.

There are a vast number of sub-grid features that can affect the surface wind speed. This study focuses on one sub-grid feature that strongly affects Cold Air Outbreaks (CAOs): cold pool formation and associated density current-driven enhancements in surface wind speed (Feingold et al., 2010; Thorpe et al., 1982). CAOs are synoptic-scale weather patterns where advection of cold, dry air masses from cold continents over relatively warm ocean causes an unstable boundary layer. They occur most frequently during the winter months in Northern Hemisphere midlatitudes. CAOs generate the largest fluxes of SH and LH on Earth (Dahlke et al., 2022; Kolstad, 2017). Fluxes in CAOs can exceed $1,000 \text{ Wm}^{-2}$ (Bane & Osgood, 1989; Bigorre et al., 2013; Marshall et al., 2009), where they account for 60%–80% of the wintertime oceanic heat loss in the Northern Hemisphere (Papritz & Spengler, 2017). Fluxes in CAO events in the Northern Hemisphere are amplified by air-sea contrast due to very cold temperatures over the land in winter and strong SST gradients associated with western boundary currents (Fletcher et al., 2016; He & Lin, 2019; Xie, 2004). While severe CAOs are seen in the Northern Hemisphere midlatitudes, CAOs can occur more frequently in the Southern Hemisphere midlatitudes when viewed as individual events. In the Southern Hemisphere midlatitudes, CAOs occur in shoulder seasons as much as they occur in winter (Fletcher et al., 2016).

Open mesoscale cellular convection (MCC) occurrence frequency increases in the post-frontal regions of CAOs (McCoy et al., 2017). This leads to strong downdrafts forming cold pools which enhance surface wind speeds (Feingold et al., 2010; Thorpe et al., 1982).

Previous work analyzing air-sea interactions as a function of GCM horizontal resolution are limited to a small number of models or regional analyses. Maloney and Chelton (2006) suggests, that climate model air-sea interaction simulations degrade with decreasing grid resolution. This result was inferred from an analysis of coupling between SST and surface wind stress in GCMs in the vicinity of strong midlatitude SST fronts (e.g., Gulf Stream, Kurushio, and Agulhas regions). Coarse spatial resolutions lead to unresolved surface temperature and pressure gradients. Pope and Stratton (2002) show that systematic errors in Hadley Center Atmospheric climate Model version 3 (HadAM3) wind speed relative to reanalysis decrease when the horizontal resolution increases, attributed to the improvement of simulated ocean eddies. By utilizing a product that aggregates microwave wind speed estimates from multiple satellites, we are able to expand our analysis over the entirety of the midlatitudes and assess a large number of GCM wind speed simulations. In this study we expand upon previous studies by examining a selection of GCMs participating in the sixth CMIP6. In the following sections, we analyze the near-surface wind bias between CMIP6 GCMs and MAC-LWP retrievals, and explore its relationship with model resolution.

2. Materials and Methods

This study compares the passive microwave-derived U_{10m} , aggregated as part of the MultiSensor Advanced Climatology of Liquid Water Path (MAC-LWP) data product (Elsaesser et al., 2017; Naud et al., 2023), to U_{10m} from CMIP6 GCMs. We focus on the midlatitudes (30°N–80°N and 30°S–60°S). While substantial surface energy fluxes occur in the tropics (Schubert et al., 2023), the observations used in this study are less reliable in regions characterized by heavy precipitation (Meissner & Wentz, 2009), so we exclude low-latitude regions. Analyses are performed as a joint function of CAO index (M) and SST gradient. We characterize the effect of resolving SST gradients and boundary layer processes on U_{10m} by examining CMIP6 GCMs with horizontal atmospheric resolutions ranging from approximately 0.25°–3.8° (Eyring et al., 2016). All data are resampled to daily-average timescales and re-gridded to the coarsest resolution across data sets (5° × 5°). Cold pools in CAOs occur on much finer scales than resolved by any GCM (Field et al., 2017), and we characterize the effect of resolving cold pools on surface wind speed in CAOs using Weather Research and Forecasting (WRF) (Skamarock et al., 2019) simulations at approximately 2 km resolution.

2.1. Cold Air Outbreak Index

We evaluate U_{10m} as a function of CAO index (M) to understand the effect of unstable boundary layers on GCM wind speed. M is defined as $M = \theta_{SST} - \theta_{850}$ where θ_{SST} is the sea surface potential temperature, and θ_{850} is the potential temperature at the 850 hPa pressure level (Fletcher et al., 2016). The metric M represents the air-sea temperature difference that is strongly influenced by CAOs. A positive M is defined as an unstable lower troposphere.

2.2. Sea Surface Temperature Gradient

To assess the signature of thermally forced winds, we evaluate the variation of U_{10m} as a function of SST gradient. SST gradient (∇SST) is calculated using the central difference method (Vazquez-Cuervo et al., 2013):

$$\nabla_x SST(i, j) = (SST(i + 1, j) - SST(i - 1, j)) / 2\Delta X$$

$$\nabla_y SST(i, j) = (SST(i, j + 1) - SST(i, j - 1)) / 2\Delta Y$$

$$|\nabla SST|(i, j) = (\nabla_x SST(i, j)^2 + \nabla_y SST(i, j)^2)^{1/2}$$

where ΔX and ΔY are the distances in km between the neighboring meridional and zonal grid points, respectively.

2.3. Observations

As mentioned above, we leverage passive microwave observations of wind from space to evaluate GCMs, as opposed to the active microwave retrievals from sun synchronous satellites used in previous work (Chelton et al., 2004; Small et al., 2008). We use these sources since microwave radiometer data might be more suitable for studying non-first-harmonic diurnally varying transient convective wind signals that would influence a daily

average computation. Passive microwave wind speed retrievals depend on the surface roughness (F. Wentz & Meissner, 2000). The algorithm to compute wind speed uses polarized brightness temperature observations and total one-way atmospheric transmittance (F. J. Wentz, 1992). Rain can interfere with the retrieval of surface roughness (Contreras & Plant, 2006). Error may also be introduced by averaging across different sensor footprints (Emery & Camps, 2017).

Passive microwave wind retrievals can be validated against buoy winds in rain-free conditions. Passive microwave retrievals show low biases compared to in-situ measurements (Mears et al., 2001; Meissner et al., 2001; F. J. Wentz, 1997; Zhang et al., 2018). Zhang et al. (2018) diagnose a mean bias <0.25 m/s and Mears et al. (2001) diagnose a mean bias <0.4 m/s for clear sky conditions.

Passive microwave retrievals of U_{10m} are ancillary variables used in the MAC-LWP climate data record (Elsaesser et al., 2017; Naud et al., 2023). MAC-LWP utilizes data from the following satellite instruments: Special Sensor Microwave Imager (SSM/I), Tropical Rainfall Measuring Mission (TRMM) Microwave Imager (TMI), Advanced Microwave Scanning Radiometer Earth Observing System (AMSR-E), WindSat, Special Sensor Microwave Imager/Sounder (SSMIS), the Advanced Microwave Scanning Radiometer 2 (AMSR-2), and Global Precipitation Measurement (GPM) Microwave Imager (GMI). At present 29 years (1988–2016) of gridded (1°) data over oceans are available. Daily-mean U_{10m} from MAC-LWP for a period of 27 years (1988–2014), set to agree with available GCM data, were used in this study. MAC-LWP passive microwave wind speed retrievals are corrected for the drifting satellite overpass times and sample the entire diurnal cycle (Elsaesser et al., 2017; Trenberth et al., 2005; F. J. Wentz, 2015) thus ensuring that the daily estimate is an average of validated windspeed retrievals (Elsaesser et al., 2017; Mears et al., 2001; Meissner et al., 2001; O'Dell et al., 2008; F. J. Wentz, 1997) and comparable to other daily-averaged cloud variables (Naud et al., 2023). Since Multi-sensor Advanced Climatology (MAC) provides an estimate of the daily-mean U_{10m} , as opposed to a retrieval at the satellite overpass time, this enables a direct comparison to CMIP6 GCM daily-averaged data without the need to implement a satellite simulator that accounts for overpass time.

The second Modern-Era Retrospective analysis for Research and Applications (MERRA2) reanalysis (Molod et al., 2015) is used to calculate M and SST gradients. The native MERRA2 resolution of $0.5^\circ \times 0.625^\circ$ was subsampled by nearest neighbor remapping to a resolution of 1° to calculate these two variables.

2.4. Global Climate Model Data

This study examines historical simulation outputs from 27 CMIP6 GCMs with horizontal atmospheric resolutions ranging from ≈ 279 km to ≈ 50 km. The resolution is calculated by $\sqrt{dx \times dy} \times 100$ km where dx and dy are the zonal, meridional grid spacing. Twenty seven years of GCM data are examined. The list of analyzed GCMs and resolutions is given in Table S1 in Supporting Information S1. The CMIP variables used for the analysis are Near-Surface Wind Speed (*sfcWind*), Sea Level Pressure (*psl*), Air Temperature (*ta*), and Surface Temperature (*ts*). The analysis of GCMs at their resolutions limits the ability to examine the effects of small-scale features on U_{10m} representation. Hence we utilize a WRF simulation at 2 km resolution to analyze sub-grid-scale features affecting U_{10m} that might be missing in GCMs, so as to understand ballpark magnitudes of surface wind underestimation that might emerge in the GCMs.

2.5. Weather Research and Forecasting Model Simulations

The Weather Research and Forecasting (WRF) model offers a flexible and computationally efficient platform to produce simulations using actual or idealized atmospheric conditions (Powers et al., 2017). This study uses the WRF model version 4.4 with two nested domains, each with 136 vertical levels. Each simulation was run for 29 hr, with data output hourly. The first 5 hr were not used to allow for model spin up. The physics schemes used in the study include the WRF Single-Moment 6-Class microphysics scheme (WSM6) (Hong & Lim, 2006), the Rapid Radiative Transfer Model for GCMs (RRTMG) for longwave and shortwave radiative schemes (Clough et al., 2005), and the Yonsei University scheme for boundary layer parameterization (Hong et al., 2006). The fifth generation European Center for Medium-Range Weather Forecasts (ECMWF) reanalysis (ERA5) 3-hourly data were used to nudge WRF simulation boundary conditions toward observations (Hersbach et al., 2020).

WRF is run over the Norwegian sea in Northern Hemisphere extratropics set to correspond to where strong CAOs were observed during the Cold-Air Outbreaks in the Marine Boundary Layer Experiment (COMBLE) field

campaign (Geerts et al., 2022) on 28th March 2020. We select this specific domain and date to examine U_{10m} in a strong CAO. Cold pools formed in this CAO allow us to examine cold pool effects on U_{10m} using WRF. We do not compare these simulations with MAC estimates but analyze the occurrence of cold pools and U_{10m} representation at very high-resolution simulations. WRF U_{10m} is qualitatively compared with SAR winds (Sikora et al., 2006). SAR data is provided by the NOAA NESDIS Center for Satellite Applications and Research.

3. Results

3.1. Surface Wind Speed Bias

U_{10m} in GCMs participating in CMIP6 is uniformly lower than observed by MAC. This appears in mean U_{10m} (Figure 1a) as well as when U_{10m} is composited on M and SST gradient (Figures 1d and 1e). Both GCM M and SST gradient medians are distributed around the values predicted by reanalysis (Figures 1b and 1c).

Observed U_{10m} is higher than GCM-predicted U_{10m} as M increases, except for a few models in the range $M < 0K$ (Figure 1d). There is a monotonic relationship between U_{10m} and M in observations and GCMs (Figure 1d).

Most GCMs are biased in U_{10m} compared to MAC throughout the range of SST gradients, except a few for which biases are small when gradients are less than 0.005 K/km (Figure 1e). The U_{10m} bias extends up to 2 m/s when composited by SST gradients. For GCMs, U_{10m} remains relatively constant for SST gradient values $> \approx 0.01$ K/km. MAC shows a positive monotonic relationship that continues through the range of SST gradients found in the study region. The range of bias in the median (Figure 1a) and when composited on M (Figure 1d) and SST gradient (Figure 1e) is greater than the range of possible microwave wind speed bias relative to in-situ observations diagnosed by previous studies (Mears et al., 2001; Zhang et al., 2018).

U_{10m} is clearly low in the 27 GCMs surveyed here at a magnitude that depends on both M and SST gradient. However, before we delve into the dependence of wind on these parameters, it is worth discussing how well GCMs represent SST gradients and CAOs. We have looked at the SST gradients and CAOs using probability density function (PDF) and spatial distribution diagnostics. Our analysis yields concise results for the U_{10m} biases. Figures 1b and 1c show the PDFs of SST gradients and M , while Figure 4, and Figures S5–S31 in Supporting Information S1 show the spatial distributions of selected M and SST gradient regimes. Observational SST gradient- M regimes broadly map with GCMs spatially (Figure 4, Figures S5–S31 in Supporting Information S1). GCMs tend to be in good agreement with observations in terms of SST gradient distributions (Figure 1b). While median M is not dramatically different from GCMs to reanalysis, the distribution of M in GCMs is skewed slightly toward higher values (Figure 1c). Persistent biases in U_{10m} may be compensated to some degree by systematic biases in GCM M . GCMs tend to have boundary layers that are relatively unstable (Figure 1c) (Qu et al., 2014) resulting in compensating errors between the frequency of occurrence of synoptic state and low U_{10m} . If the average boundary layer stability in GCMs was consistent with observations, the bias in GCM U_{10m} would be more pronounced.

3.2. Cold Pool Contribution to Surface Wind Speed

Cold pools often appear in CAOs (Papritz et al., 2019; Shapiro et al., 1987) and may be one mechanism linking boundary layer winds to CAO occurrence (Zuidema et al., 2012). Cold pools appear as pockets of enhanced wind speed in high-resolution simulations (Figure 2). Cold pools exhibit spatial scales of 10–200 km and are not resolved in most present-day GCMs (Field et al., 2017; Zuidema et al., 2017). Cold pools are driven by processes related to precipitation, clouds, and convection, all of which are largely parameterized in GCMs (Bryan et al., 2003; Sakradzija et al., 2016). Thus parametric and structural uncertainty exists in boundary layer behavior in GCM-simulated CAOs.

Our WRF simulation, run over a domain in the Norwegian sea on 28th March 2020, can resolve many cold pools (Figure 2) and enable qualitative characterization of the contribution of cold pool-induced gustiness to surface wind speed that might be underestimated in GCMs. The reasonably-high WRF horizontal resolutions enable resolving of some convective and boundary layer processes operating in cold pools (Field et al., 2017). These simulations are only exploratory and not an exhaustive evaluation of the cold pool contribution to surface wind speed across regimes and microphysical processes, which has partially been addressed elsewhere (Saggiorato et al., 2020). The GCM evaluation across the domain where the WRF analysis is performed shows underestimated U_{10m} (Figure S1 in Supporting Information S1). This analysis is in line with the global midlatitude analysis shown in Figure 1.

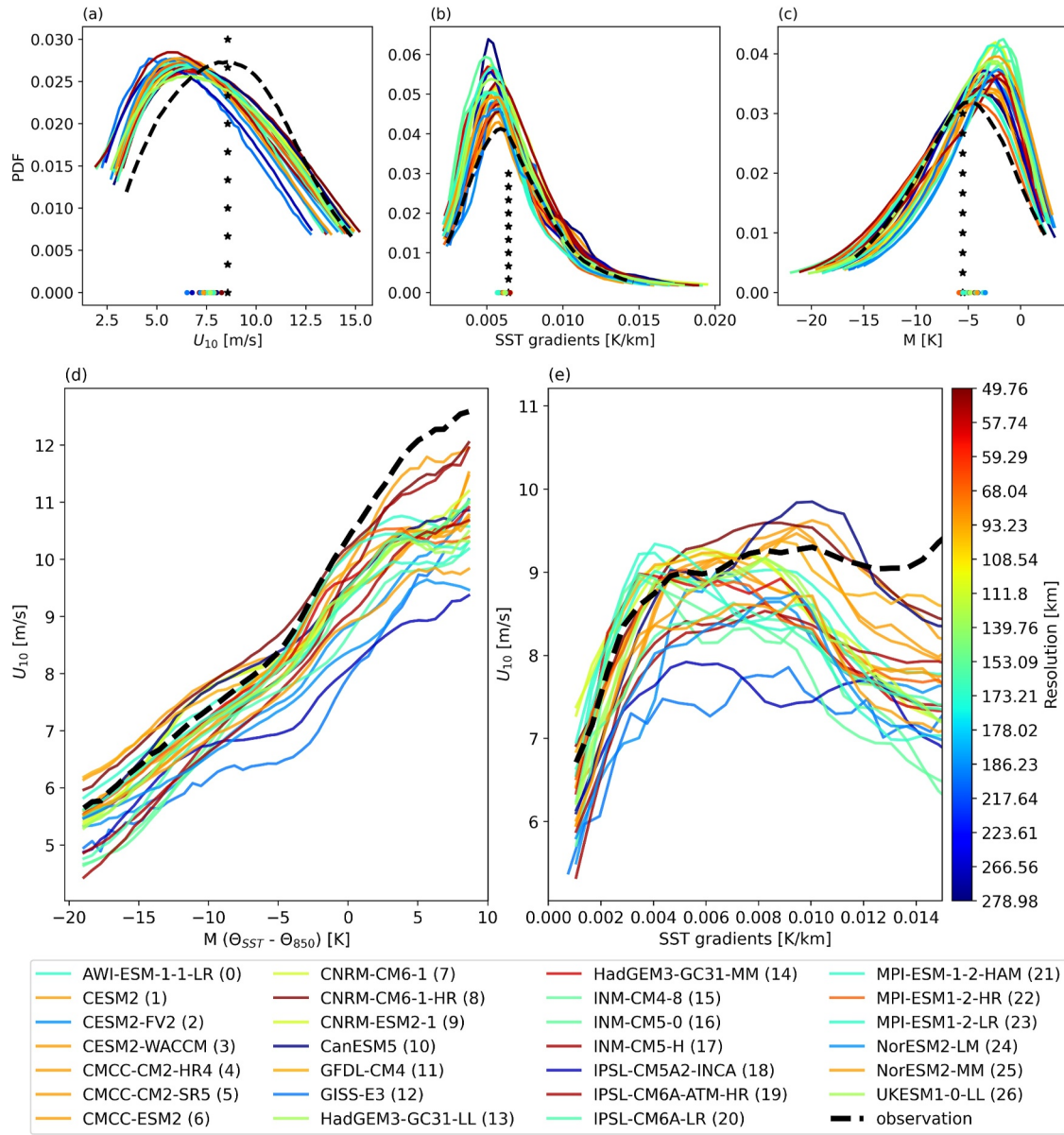


Figure 1. (a) The distribution of U_{10m} (b) the distribution of sea surface temperature (SST) gradients, and (c) the distribution of cold air outbreak index ($M = \theta_{SST} - \theta_{850}$) from observations (black dashed line) and coupled model intercomparison project global climate models (GCMs) (colored lines by horizontal resolution) over oceans between 30°N and 80°N and 30°S–60°S. Dots show the median of each GCM and the vertical star line is the observed median. (d) U_{10m} as a function of M (e) U_{10m} as a function of SST gradient.

Examination of WRF simulation output during a CAO displays cold pool formation (Figure 2). We identify cold pools as contiguous adjacent boxes of anomalously cold temperature 1–3 K colder than surrounding areas (Zuidema et al., 2012). We focus on a simulation of a CAO observed during the Cold-Air Outbreaks in the Marine Boundary Layer Experiment (COMBLE) field campaign (Geerts et al., 2022) (Figure 2). Strong downdrafts, updrafts, and precipitation can be seen in the vertical cross section along a transect from this simulation (Figure 2). Figure 2 shows enhancement of U_{10m} below the strong downdrafts and precipitation associated with the cold pools. U_{10m} enhancement is observed on the downwind side of the cold pools because of the northerly flow (Figure S2 in Supporting Information S1) (Li et al., 2014; Zuidema et al., 2012). The U_{10m} enhancement simulated in this CAO is consistent with wind speed observed by SAR (Figure 2).

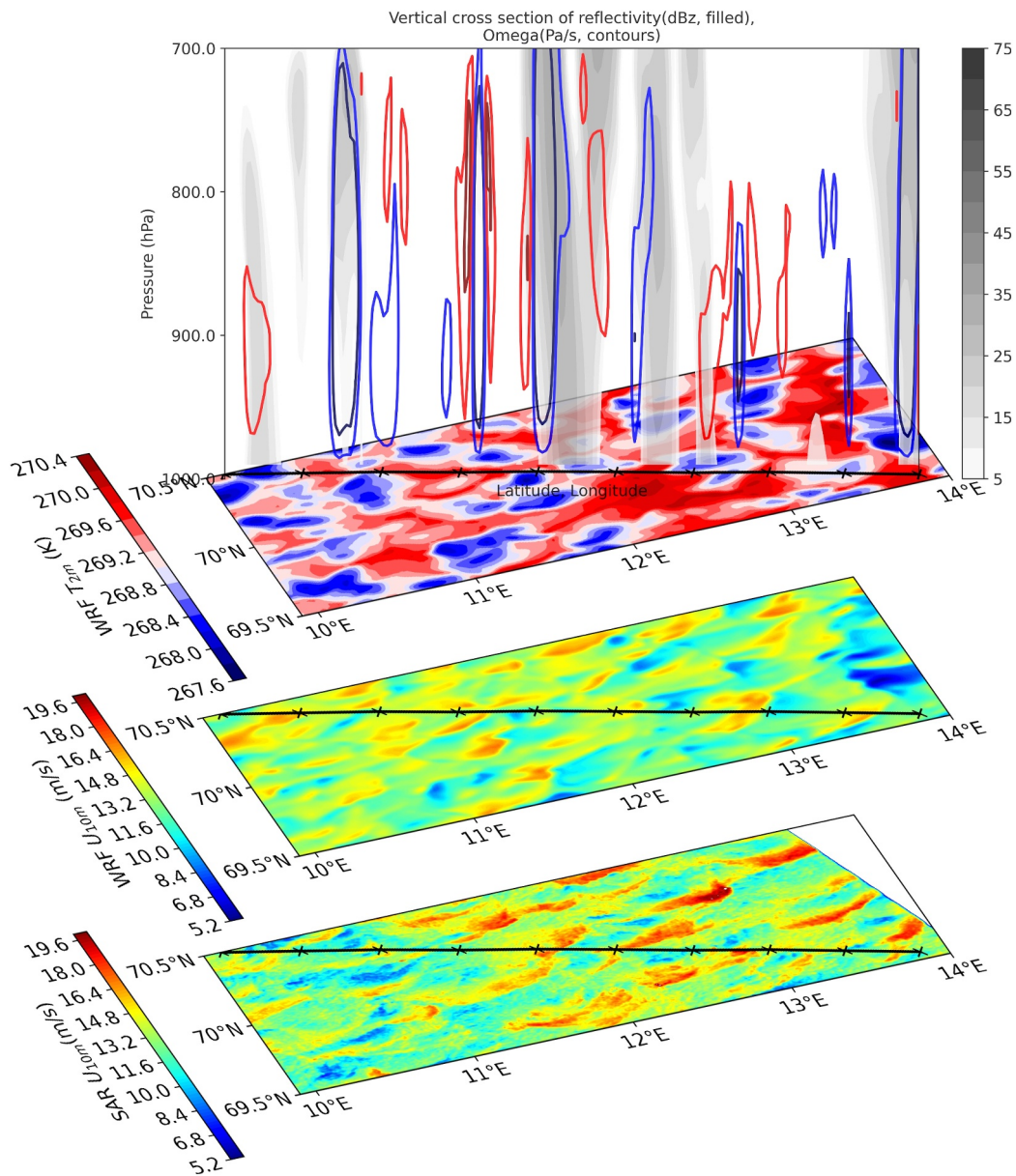


Figure 2. Weather research and forecasting (WRF) simulation of a strong cold air outbreak (CAO). A vertical cross-section along a Transect showing reflectivity (filled), downdrafts (red contours), and updrafts (blue contours), WRF 2m-Temperature, WRF U_{10m} , and synthetic aperture radar (SAR) U_{10m} . SAR data provided courtesy of NOAA NESDIS center for satellite applications and research. https://www.star.nesdis.noaa.gov/socd/mecb/sar/sarwinds_s1.php.

3.3. Resolution Dependence

We expect that the wind biases that manifest with SST gradient and M (Figure 1) largely arise from processes that operate at finer spatial and temporal scales than those resolved by GCMs (Figure 2). We analyze the resolution dependence of GCM U_{10m} and examine the dependence of this bias on the meteorological regime.

To examine the U_{10m} bias (defined $U_0 - U_m$ where U_0 and U_m denote the observation and CMIP6 U_{10m} , respectively), we stratify bias by M and SST gradient (Figure 3). Higher surface wind speed appears in CAOs and higher SST gradients in observations (Figure 3a).

U_{10m} bias tends to be higher in CAOs and at higher SST gradient (Figure 3b, Figure S4 in Supporting Information S1). When the rank regression of U_{10m} bias on GCM horizontal resolution is accounted for in bins of SST

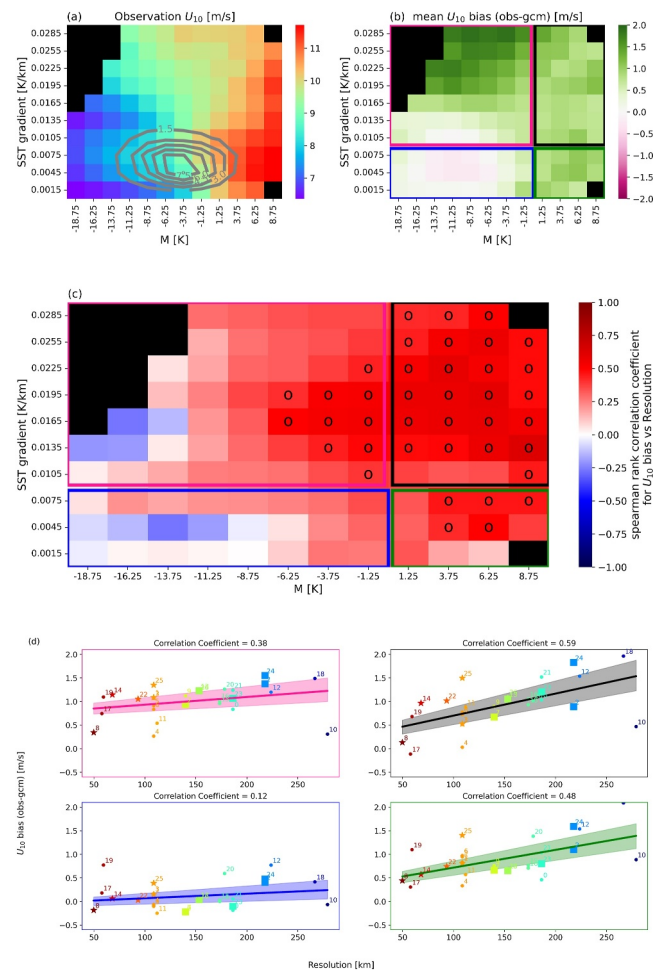


Figure 3. (a) Observed U_{10m} as a function of M and sea surface temperature (SST) gradient. Gray contours show data density percentage. (b) Average U_{10m} bias (obs—gcm) controlled for M and SST gradients. Pink, blue, black, and green colored boxes designate M and SST regimes. (c) The Spearman rank correlation coefficient for U_{10m} bias versus model horizontal resolution as a function of M and SST gradient. P-values less than 0.05 are marked with a circle. (d) Average U_{10m} bias as a function of horizontal resolution corresponding to the four regimes highlighted in (b) and (c). Stars and squares are for the available higher resolution and lower resolution versions for the same model. Points are labeled by the model number given in Figure 1. The best fit and 95% uncertainty is calculated by jackknife sampling (Tukey, 1958).

gradient and M , lower resolution corresponds to higher bias across over 80% of the bins (Figure 3c). The U_{10m} bias of each GCM for SST gradient and M bins is shown in Figure S2 in Supporting Information S1.

We aggregate our data into four M and SST gradient regimes (Figure 3d). In each regime, we characterize the relationship between U_{10m} bias and resolution by the Spearman rank-order correlation. Across regimes, the correlation is robustly greater than zero, depicting a relationship where the U_{10m} bias decreases when GCM horizontal grid resolution gets finer, although several GCMs are outliers from the trend. The strongest correlation coefficient of 0.59 corresponds to the regimes of high M and SST gradients. The high M correlations show p-values less than 0.05 and are deemed statistically significant. The correlation coefficient between U_{10m} bias and resolution in Figure 3d is consistent with each regime in Figure 3c. The presence of outliers in the relationship between bias in U_{10m} and horizontal resolution is expected. Given the drastically different model families considered in this study, it is not surprising that completely different parameterization and parameterization structures give rise to different U_{10m} bias dependence on resolution (Moreno-Chamarro et al., 2022).

We characterize the regions that are affected by wind speed bias by examining the spatial distribution of the four regimes of M and SST gradient (Figure 4, Figures S5–S31 in Supporting Information S1). The highest frequency

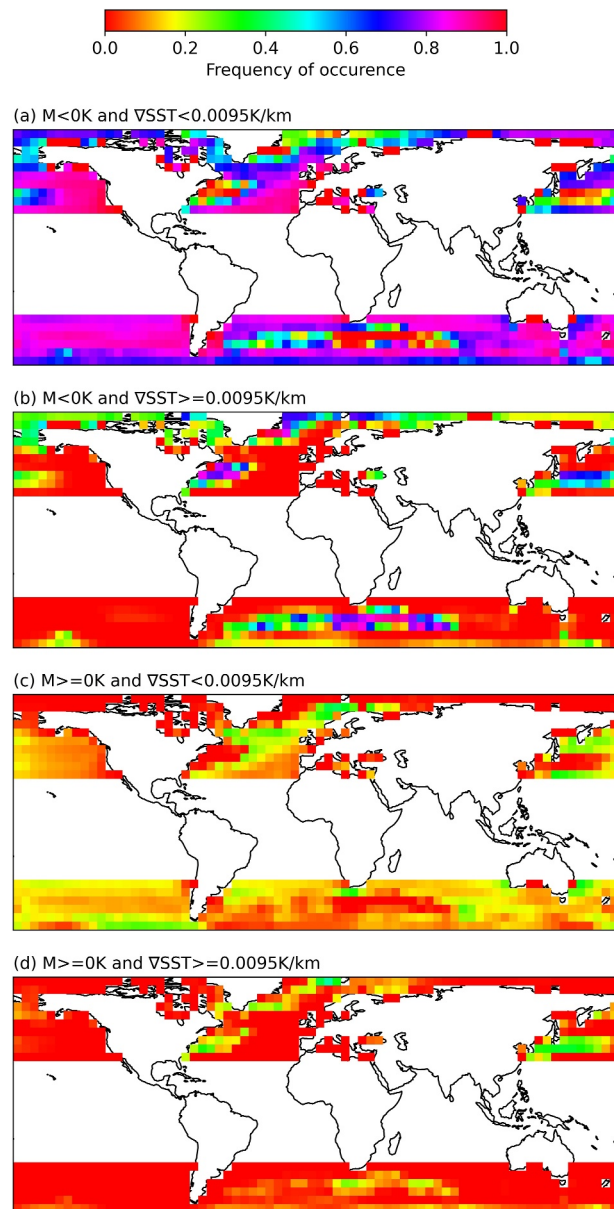


Figure 4. Relative frequency of occurrence when (a) $M < 0$ K and sea surface temperature (SST) gradient < 0.0095 K/km (blue box in Figures 3b–3d) (b) $M < 0$ K and SST gradient > 0.0095 K/km (pink box in Figures 3b–3d) (c) $M > 0$ K and SST gradient < 0.0095 K/km (green box in Figures 3b–3d) (d) $M > 0$ K and SST gradient > 0.0095 K/km (black box in Figures 3b–3d).

of occurrence of high SST gradients and unstable boundary layers are over the western boundary currents in the study region: the Gulf stream, Agulhas current, and Kuroshio current (Figure 4d). More than 57% of bins in each of the regimes with a high frequency of occurrence in western boundary currents (Figures 4b and 4d) show positive monotonic relationships between U_{10m} and grid resolution (Figure 3c). This is important to our understanding of how coarse-resolution global models predict climate because the U_{10m} bias in the western boundary currents affect the simulation of LH and SH fluxes (Alexander & Scott, 1997). Additionally, heat flux simulations in the western boundary currents affect the simulation of the thermohaline circulation (Cai & Godfrey, 1995; Delworth & Greatbatch, 2000) in GCMs. The effect of the Gulf Stream on the troposphere is significant, and accurate prediction within the regions of these western boundary currents is important (Minobe et al., 2008).

4. Conclusion

This study evaluates CMIP6 GCM U_{10m} in the midlatitudes (30°N–80°N and 30°S–60°S) against the MAC climate data record. We find that the U_{10m} is underestimated compared to MAC estimates across all 27 CMIP6 GCMs considered in this study (Figures 1d and 1e). This GCM bias is concerning because U_{10m} is a critical measure of the atmospheric state and governs air-sea exchange and affects boundary layer evolution (Hartmann, 2016; Saggiolato et al., 2020).

One possible reason for biased surface wind in GCMs is a poor representation of the subgrid processes that contribute to cold pool formation (Field et al., 2017) and systematic high wind gusts. We integrated WRF simulations in CAOs to evaluate the impact of these km-scale processes (Figure 2). Our case study WRF simulations show enhanced U_{10m} in cold pool downdrafts in CAOs. This is supported by previous studies examining observations (Zuidema et al., 2012) and high-resolution simulations of cold pools (Fiévet et al., 2023). Across GCMs and observations, stronger CAOs correspond to stronger surface winds (Figures 1d and 3a). Broadly, higher resolution models are in closer agreement with observations at a fixed CAO index (Figure 3c).

Another possible reason for the bias in the GCM U_{10m} stems from GCMs only crudely resolving SST gradients that in turn modulate surface wind speed U_{10m} (Chelton, 2005; Chelton & Wentz, 2005; LaCasse et al., 2006). Across GCMs and observations, larger SST gradients correspond to stronger surface winds, and higher resolution models tend to be in closer agreement with observations at a fixed SST gradient (Figures 1e and 3c).

We find that U_{10m} bias decreases with GCM horizontal grid resolution (Figures 3c and 3d). Surface wind speed depends strongly on M and SST gradient (Figures 1d and 1e). We evaluate resolution dependence controlling for M and SST gradients (Figures 3b and 3c). We find that the highest correlations between the U_{10m} bias and the GCM horizontal resolutions are over the most unstable boundary layers with the highest SST gradients. These regimes correspond to the western boundary currents (Figures 3d and 4) which affect the representation of thermohaline circulation (Cai & Godfrey, 1995; Delworth & Greatbatch, 2000). This supports previous work suggesting that GCM horizontal resolution may play an important part in climate predictability through features such as the thermohaline through the representation of U_{10m} and associated surface fluxes (Bellucci et al., 2021; Roberts et al., 2020).

Data Availability Statement

All CMIP data are available at CMIP6 Earth System Grid Federation (2023). MAC wind data can be accessed at Naud et al. (2023). MERRA-2 data are available at GES DISC Data set: MERRA-2 inst1_2d_asm_Nx: 2d, 1-Hourly, Instantaneous, Single-Level, Assimilation, Single-Level Diagnostics V5.12.4 (M2I1NXASM 5.12.4) (2015) and GES DISC Data set: MERRA-2 inst3_3d_asm_Np: 3d, 3-Hourly, Instantaneous, Pressure-Level, Assimilation, Assimilated Meteorological Fields V5.12.4 (M2I3NPASM 5.12.4) (2015). SAR wind data provided courtesy of NOAA NESDIS Center for Satellite Applications and Research (NOAA STAR, 2024).

Acknowledgments

We thank our editor, Hui Su, and the two reviewers, Dr. R. J. Small and the anonymous reviewer, for their invaluable feedback and contributions to improving the paper. We would like to acknowledge the use of computational resources (doi:10.5065/D6RX99HX) at the NCAR-Wyoming Supercomputing Center provided by the National Science Foundation and the State of Wyoming and supported by NCAR's Computational and Information Systems Laboratory under allocation WYOM0131. The contributions of GE were additionally supported by the NASA Modeling, Analysis, and Prediction program and APAM GISS Co-Op 80NSSC18M0133, and NASA Precipitation Measurement Mission Grant 80NSSC22K0609. GW and DTM's efforts were supported under NASA Precipitation Measurement Mission Grant 80NSSC22K0599.

References

- Alexander, M. A., & Scott, J. D. (1997). Surface flux variability over the North Pacific and North Atlantic Oceans. *Journal of Climate*, 10(11), 2963–2978. [https://doi.org/10.1175/1520-0442\(1997\)010<2963:SFVOTN>2.0.CO;2](https://doi.org/10.1175/1520-0442(1997)010<2963:SFVOTN>2.0.CO;2)
- Bane, J. M., & Osgood, K. E. (1989). Wintertime air-sea interaction processes across the Gulf Stream. *Journal of Geophysical Research*, 94(C8), 10755–10772. <https://doi.org/10.1029/JC094iC08p10755>
- Bellucci, A., Athanasiadis, P. J., Scoccimarro, E., Ruggieri, P., Gualdi, S., Fedele, G., et al. (2021). Air-sea interaction over the Gulf Stream in an ensemble of highresmp present climate simulations. *Climate Dynamics*, 56(7–8), 2093–2111. <https://doi.org/10.1007/s00382-020-05573-z>
- Bigorre, S. P., Weller, R. A., Edson, J. B., & Ware, J. D. (2013). A surface Mooring for air-sea interaction research in the gulf stream. Part II: Analysis of the observations and their accuracies. *Journal of Atmospheric and Oceanic Technology*, 30(3), 450–469. <https://doi.org/10.1175/JTECH-D-12-00078.1>
- Bodas-Salcedo, A., Mulcahy, J. P., Andrews, T., Williams, K. D., Ringer, M. A., Field, P. R., & Elsaesser, G. S. (2019). Strong dependence of atmospheric feedbacks on mixed-phase microphysics and aerosol-cloud interactions in HadGEM3. *Journal of Advances in Modeling Earth Systems*, 11(6), 1735–1758. <https://doi.org/10.1029/2019MS001688>
- Bryan, G. H., Wyngaard, J. C., & Fritsch, J. M. (2003). Resolution requirements for the simulation of deep moist convection. *Monthly Weather Review*, 131(10), 2394–2416. [https://doi.org/10.1175/1520-0493\(2003\)131<2394:RRFTSO>2.0.CO;2](https://doi.org/10.1175/1520-0493(2003)131<2394:RRFTSO>2.0.CO;2)
- Cai, W., & Godfrey, S. J. (1995). Surface heat flux parameterizations and the variability of thermohaline circulation. *Journal of Geophysical Research*, 100(C6), 10679–10692. <https://doi.org/10.1029/95JC00587>
- Chelton, D. B. (2005). The impact of SST specification on ECMWF surface wind stress fields in the eastern tropical Pacific. *Journal of Climate*, 18(4), 530–550. <https://doi.org/10.1175/JCLI-3275.1>
- Chelton, D. B., Schlax, M. G., Freilich, M. H., & Milliff, R. F. (2004). Satellite measurements reveal persistent small-scale features in ocean winds. *Science*, 303(5660), 978–983. <https://doi.org/10.1126/science.1091901>

- Chelton, D. B., & Wentz, F. J. (2005). Global microwave satellite observations of sea surface temperature for numerical weather prediction and climate research. *Bulletin of the American Meteorological Society*, 86(8), 1097–1116. <https://doi.org/10.1175/BAMS-86-8-1097>
- Chu, P. C. (1989). Relationship between thermally forced surface wind and sea surface temperature gradient. *Pure and Applied Geophysics PAGEOPH*, 130(1), 31–45. <https://doi.org/10.1007/BF00877735>
- Clough, S., Shephard, M., Mlawer, E., Delamere, J., Iacono, M., Cady-Pereira, K., et al. (2005). Atmospheric radiative transfer modeling: A summary of the AER codes. *Journal of Quantitative Spectroscopy and Radiative Transfer*, 91(2), 233–244. <https://doi.org/10.1016/j.jqsrt.2004.05.058>
- CMIP6. (2023). CMIP6 earth system grid federation. [Dataset]. <https://doi.org/10.5194/gmd-9-3447-2016>
- Contreras, R. F., & Plant, W. J. (2006). Surface effect of rain on microwave backscatter from the ocean: Measurements and modeling. *Journal of Geophysical Research*, 111(C8). <https://doi.org/10.1029/2005JC003356>
- Dahlke, S., Solbès, A., & Maturilli, M. (2022). Cold air outbreaks in Fram strait: Climatology, trends, and observations during an extreme season in 2020. *Journal of Geophysical Research: Atmospheres*, 127(3), e2021JD035741. <https://doi.org/10.1029/2021JD035741>
- Delworth, T. L., & Greatbatch, R. J. (2000). Multidecadal thermohaline circulation variability driven by atmospheric surface flux forcing. *Journal of Climate*, 13(9), 1481–1495. [https://doi.org/10.1175/1520-0442\(2000\)013<1481:MTCVDB>2.0.CO;2](https://doi.org/10.1175/1520-0442(2000)013<1481:MTCVDB>2.0.CO;2)
- Elsaesser, G. S., & Kummerow, C. D. (2013). A multisensor observational depiction of the transition from light to heavy rainfall on subdaily time scales. *Journal of the Atmospheric Sciences*, 70(7), 2309–2324. Place: Boston MA, USA Publisher: American Meteorological Society. <https://doi.org/10.1175/JAS-D-12-0210.1>
- Elsaesser, G. S., O'Dell, C. W., Lebsock, M. D., Bennartz, R., Greenwald, T. J., & Wentz, F. J. (2017). The multisensor advanced climatology of liquid water path (MAC-LWP). *Journal of Climate*, 30(24), 10193–10210. <https://doi.org/10.1175/JCLI-D-16-0902.1>
- Emery, W., & Camps, A. (2017). Microwave radiometry. In *Introduction to satellite remote sensing* (pp. 131–290). Elsevier. <https://doi.org/10.1016/B978-0-12-809254-5.00004-X>
- Evan, A. T. (2018). Surface winds and dust biases in climate models. *Geophysical Research Letters*, 45(2), 1079–1085. <https://doi.org/10.1002/2017GL076353>
- Eyring, V., Bony, S., Meehl, G. A., Senior, C. A., Stevens, B., Stouffer, R. J., & Taylor, K. E. (2016). Overview of the coupled model inter-comparison project phase 6 (CMIP6) experimental design and organization. *Geoscientific Model Development*, 9(5), 1937–1958. <https://doi.org/10.5194/gmd-9-1937-2016>
- Feingold, G., Koren, I., Wang, H., Xue, H., & Brewer, W. A. (2010). Precipitation-generated oscillations in open cellular cloud fields. *Nature*, 466(7308), 849–852. <https://doi.org/10.1038/nature09314>
- Ferrari, R., & Wunsch, C. (2009). Ocean circulation kinetic energy: Reservoirs, sources, and sinks. *Annual Review of Fluid Mechanics*, 41(1), 253–282. <https://doi.org/10.1146/annurev.fluid.40.111406.102139>
- Field, P. R., Brozková, R., Chen, M., Dudhia, J., Lac, C., Hara, T., et al. (2017). Exploring the convective grey zone with regional simulations of a cold air outbreak. *Quarterly Journal of the Royal Meteorological Society*, 143(707), 2537–2555. <https://doi.org/10.1002/qj.3105>
- Fiévet, R., Meyer, B., & Haerter, J. O. (2023). On the sensitivity of convective cold pools to mesh resolution. *Journal of Advances in Modeling Earth Systems*, 15(8), e2022MS003382. <https://doi.org/10.1029/2022MS003382>
- Fletcher, J., Mason, S., & Jakob, C. (2016). The Climatology, meteorology, and boundary layer structure of marine cold air outbreaks in both hemispheres. *Journal of Climate*, 29(6), 1999–2014. <https://doi.org/10.1175/JCLI-D-15-0268.1>
- Fu, L.-L., Lee, T., Liu, W. T., & Kwok, R. (2019). 50 Years of satellite remote sensing of the ocean. *Meteorological Monographs*, 59(5.1–5.46), 51–546. Place: Boston MA, USA Publisher: American Meteorological Society. <https://doi.org/10.1175/AMSMONOGRAPH5-D-18-0010.1>
- Geerts, B., Giangrande, S. E., McFarquhar, G. M., Xue, L., Abel, S. J., Comstock, J. M., et al. (2022). The Comble campaign: A study of marine boundary layer clouds in arctic cold-air outbreaks. *Bulletin of the American Meteorological Society*, 103(5), E1371–E1389. <https://doi.org/10.1175/bams-d-21-0044.1>
- GES DISC Dataset. (2015a). MERRA-2 inst1_2d_asm_nx: 2d, 1-Hourly, instantaneous, single-level, assimilation, single-level diagnostics V5.12.4 (M2I1NXASM 5.12.4). [Dataset]. <https://doi.org/10.5067/3Z173KIE2TPD>
- GES DISC Dataset. (2015b). MERRA-2 inst3_3d_asm_np: 3d, 3-hourly, instantaneous, pressure-Level, assimilation, assimilated meteorological fields V5.12.4 (M2I3NPASM 5.12.4). [Dataset]. <https://doi.org/10.5067/QBZ6MG944HW0>
- Hartmann, D. L. (2016). *Global physical climatology (second ed.)* (Nos. Book, Whole). Elsevier. Retrieved from https://uwoy.summon.serialssolutions.com/2.0.0/link/0/eLvHCXmWY2AwNtZ0EUrEywTUAn2ZkmG1mmpqbGqZZWKakJmIglQkpaYZpViiHjvLABvZRojhi3jEWhEetSRc0NzM3NgxacWYgs6IEKtDHJ1snf3zuYmYEV2KI2AG8SdnIGrYMur0SuX9wEGVhTQZsOhBiYUvOEGdjdwdftVgozSPoC27T5RWCEgpcC04msIEJIWMHL95MLhZhkiYc3K9QAA1zhWSE0IEGWTFXEGcPXZCd8dDBmvgkYPPfCNGoMjAWY-BNBC1yzysBb4ZLkWBQSDZNS0s0zRkSK4yNTEXT040MU02M7JISUo2MAcdUy_JlIbdMCicEtIMXMAWAHRMQYabPaSoNFUWEGxy4DABAFNgSc
- He, J., & Lin, X. (2019). Co-Variation of the surface wind speed and the sea surface temperature over mesoscale eddies in the gulf stream region: Momentum vertical mixing aspect. *Journal of Oceanology and Limnology*, 37(4), 1154–1164. <https://doi.org/10.1007/s00343-019-8094-0>
- Hersbach, H., Bell, B., Berrisford, P., Hirahara, S., Horányi, A., Muñoz-Sabater, J., et al. (2020). The ERA5 global reanalysis. *Quarterly Journal of the Royal Meteorological Society*, 146(730), 1999–2049. <https://doi.org/10.1002/qj.3803>
- Hong, S.-Y., & Lim, J.-O. J. (2006). The WRF single-moment 6-Class microphysics scheme (WSM6). *Asia-Pacific Journal of Atmospheric Sciences*, 42, 129–151.
- Hong, S.-Y., Noh, Y., & Dudhia, J. (2006). A new vertical diffusion package with an explicit treatment of entrainment processes. *Monthly Weather Review*, 134(9), 2318–2341. <https://doi.org/10.1175/MWR3199.1>
- Kolstad, E. W. (2017). Higher ocean wind speeds during marine cold air outbreaks. *Quarterly Journal of the Royal Meteorological Society*, 143(706), 2084–2092. <https://doi.org/10.1002/qj.3068>
- Krishnan, A., & Bhaskaran, P. K. (2020). Performance of CMIP5 wind speed from global climate models for the Bay of Bengal region. *International Journal of Climatology*, 40(7), 3398–3416. <https://doi.org/10.1002/joc.6404>
- LaCasse, K. M., Lapenta, W. M., Lazarus, S. M., Splitt, M. E., Jedlovec, G. J., & Haines, S. L. (2006). 1.3 The impact of Modis SST composites on short-term regional forecasts.
- Li, Z., Zuidema, P., & Zhu, P. (2014). Simulated convective invigoration processes at trade wind cumulus cold pool boundaries. *Journal of the Atmospheric Sciences*, 71(8), 2823–2841. <https://doi.org/10.1175/JAS-D-13-0184.1>
- Maloney, E. D., & Chelton, D. B. (2006). An Assessment of the sea surface temperature influence on surface wind stress in numerical weather prediction and climate models. *Journal of Climate*, 19(12), 2743–2762. <https://doi.org/10.1175/JCLI3728.1>
- Marshall, J., Andersson, A., Bates, N., Dewar, S., Doney, S., Edson, J., et al. (2009). The Climode field campaign. *Bulletin of the American Meteorological Society*, 90(9), 1337–1350. <https://doi.org/10.1175/2009bams2706.1>

- McCoy, I. L., Wood, R., & Fletcher, J. K. (2017). Identifying meteorological controls on open and closed mesoscale cellular convection associated with marine cold air outbreaks. *Journal of Geophysical Research: Atmospheres*, 122(21), 11678–11702. <https://doi.org/10.1002/2017JD027031>
- McMonigal, K., Larson, S., Hu, S., & Kramer, R. (2023). Historical changes in wind-driven ocean circulation can accelerate global warming. *Geophysical Research Letters*, 50(4). <https://doi.org/10.1029/2023GL102846>
- Mears, C. A., Smith, D. K., & Wentz, F. J. (2001). Comparison of special sensor microwave imager and buoy-measured wind speeds from 1987 to 1997. *Journal of Geophysical Research*, 106(C6), 11719–11729. <https://doi.org/10.1029/1999JC000097>
- Meissner, T., Smith, D., & Wentz, F. (2001). A 10 year intercomparison between collocated Special Sensor Microwave Imager oceanic surface wind speed retrievals and global analyses. *Journal of Geophysical Research*, 106(C6), 11731–11742. <https://doi.org/10.1029/1999JC000098>
- Meissner, T., & Wentz, F. J. (2009). Wind-Vector retrievals under rain with passive satellite microwave radiometers. *IEEE Transactions on Geoscience and Remote Sensing*, 47(9), 3065–3083. Conference Name: IEEE Transactions on Geoscience and Remote Sensing. <https://doi.org/10.1109/TGRS.2009.2027012>
- Minobe, S., Kuwano-Yoshida, A., Komori, N., Xie, S.-P., & Small, R. J. (2008). Influence of the gulf stream on the troposphere. *Nature*, 452(7184), 206–209. <https://doi.org/10.1038/nature06690>
- Molod, A., Takacs, L., Suarez, M., & Bacmeister, J. (2015). Development of the GEOS-5 atmospheric general circulation model: Evolution from MERRA to MERRA2. *Geoscientific Model Development*, 8(5), 1339–1356. <https://doi.org/10.5194/gmd-8-1339-2015>
- Moreno-Chamarro, E., Caron, L.-P., Loosveldt Tomas, S., Vegas-Regidor, J., Gutjahr, O., Moine, M.-P., et al. (2022). Impact of increased resolution on long-standing biases in highresnip-primavera climate models. *Geoscientific Model Development*, 15(1), 269–289. <https://doi.org/10.5194/gmd-15-269-2022>
- Morim, J., Hemer, M., Andutta, F., Shimura, T., & Cartwright, N. (2020). Skill and uncertainty in surface wind fields from general circulation models: Intercomparison of bias between AGCM, AOGCM and ESM global simulations. *International Journal of Climatology*, 40(5), 2659–2673. <https://doi.org/10.1002/joc.6357>
- Naud, C. M., Elsaesser, G. S., & Booth, J. F. (2023). Dominant cloud controlling factors for low-level cloud fraction: Subtropical versus extratropical oceans [Dataset]. *Geophysical Research Letters*, 50(19), e2023GL104496. <https://doi.org/10.1029/2023GL104496>
- NOAA STAR. (2024). Noaa star. [Dataset]. https://www.star.nesdis.noaa.gov/socd/mecb/sar/sarwinds_s1.php
- O'Dell, C. W., Wentz, F. J., & Bennartz, R. (2008). Cloud Liquid water Path from satellite-based passive microwave observations: A new Climatology over the global oceans. *Journal of Climate*, 21(8), 1721–1739. <https://doi.org/10.1175/2007JCLI1958.1>
- O'Neill, L. W., Chelton, D. B., & Esbensen, S. K. (2010). The effects of SST-induced surface wind speed and direction gradients on midlatitude surface vorticity and divergence. *Journal of Climate*, 23(2), 255–281. <https://doi.org/10.1175/2009JCLI2613.1>
- Papritz, L., Rouges, E., Aemisegger, F., & Wernli, H. (2019). On the thermodynamic preconditioning of Arctic air masses and the role of tropopause polar vortices for cold air outbreaks from Fram strait. *Journal of Geophysical Research: Atmospheres*, 124(21), 11033–11050. <https://doi.org/10.1029/2019JD030570>
- Papritz, L., & Spengler, T. (2017). A Lagrangian Climatology of wintertime cold air outbreaks in the Irminger and Nordic seas and their role in shaping air–sea heat fluxes. *Journal of Climate*, 30(8), 2717–2737. <https://doi.org/10.1175/jcli-d-16-0605.1>
- Pope, V., & Stratton, R. (2002). The processes governing horizontal resolution sensitivity in a climate model. *Climate Dynamics*, 19(3), 211–236. <https://doi.org/10.1007/s00382-001-0222-8>
- Possner, A., & Caldeira, K. (2017). Geophysical potential for wind energy over the open oceans. *Proceedings of the National Academy of Sciences*, 114(43), 201705710–201711343. <https://doi.org/10.1073/pnas.1705710114>
- Powers, J. G., Klemp, J. B., Skamarock, W. C., Davis, C. A., Dudhia, J., Gill, D. O., et al. (2017). The weather research and forecasting model: Overview, system efforts, and future directions. *Bulletin of the American Meteorological Society*, 98(8), 1717–1737. <https://doi.org/10.1175/BAMS-D-15-00308.1>
- Qu, X., Hall, A., Klein, S. A., & Caldwell, P. M. (2014). The strength of the tropical inversion and its response to climate change in 18 CMIP5 models. *Climate Dynamics*, 45(1–2), 375–396. <https://doi.org/10.1007/s00382-014-2441-9>
- Roberts, M. J., Jackson, L. C., Roberts, C. D., Meccia, V., Docquier, D., Koenig, T., et al. (2020). Sensitivity of the Atlantic meridional overturning circulation to model resolution in CMIP6 highres simulations and implications for future changes. *Journal of Advances in Modeling Earth Systems*, 12(8), e2019MS002014. <https://doi.org/10.1029/2019ms002014>
- Saggiorato, B., Nuijens, L., Siebesma, A. P., de Roode, S., Sandu, I., & Papritz, L. (2020). The influence of convective momentum transport and vertical wind shear on the evolution of a cold air outbreak. *Journal of Advances in Modeling Earth Systems*, 12(6), e2019MS001991. <https://doi.org/10.1029/2019MS001991>
- Sakradzija, M., Seifert, A., & Dipankar, A. (2016). A stochastic scale-aware parameterization of shallow cumulus convection across the convective gray zone. *Journal of Advances in Modeling Earth Systems*, 8(2), 786–812. <https://doi.org/10.1002/2016MS000634>
- Schubert, R., Vergara, O., & Gula, J. (2023). The open ocean kinetic energy cascade is strongest in late winter and spring. *Communications Earth & Environment*, 4(1), 1–8. Number: 1 Publisher: Nature Publishing Group. <https://doi.org/10.1038/s43247-023-01111-x>
- Seo, H., O'Neill, L. W., Bourassa, M. A., Czaja, A., Drushka, K., Edson, J. B., et al. (2023). Ocean mesoscale and frontal-scale Ocean–atmosphere interactions and influence on large-scale climate: A review. *Journal of Climate*, 36(7), 1981–2013. <https://doi.org/10.1175/JCLI-D-21-0982.1>
- Shapiro, M. A., Hampel, T., & Krueger, A. J. (1987). The Arctic tropopause fold. *Monthly Weather Review*, 115(2), 444–454. [https://doi.org/10.1175/1520-0493\(1987\)115\(0444:TATF\)2.0.CO;2](https://doi.org/10.1175/1520-0493(1987)115(0444:TATF)2.0.CO;2)
- Shen, C., Zha, J., Li, Z., Azorin-Molina, C., Deng, K., Minola, L., & Chen, D. (2022). Evaluation of global terrestrial near-surface wind speed simulated by CMIP6 models and their future projections. *Annals of the New York Academy of Sciences*, 1518(1), 249–263. <https://doi.org/10.1111/nyas.14910>
- Sikora, T. D., Young, G. S., & Winstead, N. S. (2006). A Novel approach to marine wind speed assessment using synthetic aperture Radar. *Weather and Forecasting*, 21(1), 109–115. <https://doi.org/10.1175/waf904.1>
- Skamarock, W. C., Klemp, J. B., Dudhia, J., Gill, D. O., Liu, Z., Berner, J., et al. (2019). A description of the advanced research WRF version 4. *NCAR tech. note ncar/tm-556+ str*, 145.
- Small, R., de Szoeke, S., Xie, S., O'Neill, L., Seo, H., Song, Q., et al. (2008). Air–sea interaction over ocean fronts and eddies. *Dynamics of Atmospheres and Oceans*, 45(3–4), 274–319. <https://doi.org/10.1016/j.dynatmoce.2008.01.001>
- Thorpe, A. J., Miller, M. J., & Moncrieff, M. W. (1982). Two-dimensional convection in non-constant shear: A model of mid-latitude squall lines. *Quarterly Journal of the Royal Meteorological Society*, 108(458), 739–762. <https://doi.org/10.1002/qj.49710845802>
- Trenberth, K. E., Fasullo, J., & Smith, L. (2005). Trends and variability in column-integrated atmospheric water vapor. *Climate Dynamics*, 24(7–8), 741–758. <https://doi.org/10.1007/s00382-005-0017-4>
- Tukey, J. (1958). Bias and confidence in not quite large samples. *The Annals of Mathematical Statistics*, 29, 614.

- Vazquez-Cuervo, J., Dewitte, B., Chin, T. M., Armstrong, E. M., Purca, S., & Alburquerque, E. (2013). An analysis of SST gradients off the Peruvian coast: The impact of going to higher resolution. *Remote Sensing of Environment*, 131, 76–84. <https://doi.org/10.1016/j.rse.2012.12.010>
- Wentz, F., & Meissner, T. (2000). *AMSR ocean algorithm, algorithm theoretical basis document. Algorithm theory. Basis doc. 121599A-1*. Remote Sens. Syst., Santa Rosa.
- Wentz, F. J. (1992). Measurement of oceanic wind vector using satellite microwave radiometers. *IEEE Transactions on Geoscience and Remote Sensing*, 30(5), 960–972. <https://doi.org/10.1109/36.175331>
- Wentz, F. J. (1997). A well-calibrated ocean algorithm for special sensor microwave/imager. *Journal of Geophysical Research*, 102(C4), 8703–8718. <https://doi.org/10.1029/96JC01751>
- Wentz, F. J. (2015). A 17-Yr climate record of environmental parameters derived from the tropical Rainfall measuring mission (TRMM) microwave imager. *Journal of Climate*, 28(17), 6882–6902. <https://doi.org/10.1175/JCLI-D-15-0155.1>
- Wentz, F. J., & Ricciardulli, L. (2011). Comment on “global trends in wind speed and wave height”. *Science*, 334(6058), 905. <https://doi.org/10.1126/science.1210317>
- Wentz, F. J., Ricciardulli, L., Rodriguez, E., Stiles, B. W., Bourassa, M. A., Long, D. G., et al. (2017). Evaluating and extending the ocean Wind climate data record. *IEEE Journal of Selected Topics in Applied Earth Observations and Remote Sensing*, 10(5), 2165–2185. <https://doi.org/10.1109/JSTARS.2016.2643641>
- Xie, S.-P. (2004). Satellite observations of cool ocean–atmosphere interaction. *Bulletin of the American Meteorological Society*, 85(2), 195–208. <https://doi.org/10.1175/BAMS-85-2-195>
- Young, I. R., Babanin, A. V., & Zieger, S. (2011). Response to comment on “global trends in wind speed and wave height”. *Science*, 334(6058), 905. <https://doi.org/10.1126/science.1210548>
- Young, I. R., Zieger, S., & Babanin, A. V. (2011). Global trends in wind speed and wave height. *Science*, 332(6028), 451–455. <https://doi.org/10.1126/science.1197219>
- Zhang, L., Shi, H., Wang, Z., Yu, H., Yin, X., & Liao, Q. (2018). Comparison of wind speeds from space borne microwave radiometers with in situ observations and ECMWF data over the global ocean. *Remote Sensing*, 10(3), 425. <https://doi.org/10.3390/rs10030425>
- Zuidema, P., Li, Z., Hill, R. J., Bariteau, L., Rilling, B., Fairall, C., et al. (2012). On trade wind cumulus cold pools. *Journal of the Atmospheric Sciences*, 69(1), 258–280. <https://doi.org/10.1175/JAS-D-11-0143.1>
- Zuidema, P., Torri, G., Muller, C., & Chandra, A. (2017). A survey of precipitation-induced atmospheric cold pools over oceans and their interactions with the larger-scale environment. *Surveys in Geophysics*, 38(6), 1283–1305. <https://doi.org/10.1007/s10712-017-9447-x>